Mechatronics 24 (2014) 1050–1058

Contents lists available at ScienceDirect

Mechatronics

journal homepage: www.elsevier.com/locate/mechatronics

Winding distribution effects on induction motor rotor fault diagnosis

C. Pezzani *, G. Bossio, C. De Angelo

Consejo Nacional de Investigaciones Científicas y Técnicas (CONICET), Argentina
Grupo de Electrónica Aplicada, Facultad de Ingeniería, Universidad Nacional de Río Cuarto, Ruta Nac. No. 36 km 601, X5804BYA Río Cuarto, Córdoba, Argentina

ARTICLE INFO

Article history:
Received 1 February 2013
Revised 17 August 2013
Accepted 10 September 2013
Available online 18 October 2013

Keywords:
Broken bars
Induction motor
MCSA
WFA
Winding distribution
Fault diagnosis

ABSTRACT

The sidebands around stator currents harmonics as a potential tool for supporting the diagnosis of rotor faults in induction motors are analyzed in this paper. The presence of broken bars introduces high frequency components in the machine currents spectrum in addition to the characteristic sidebands around the fundamental component. These additional components are due to the interaction between, rotor asymmetry and either the voltage harmonics, or winding distribution, or rotor slots. In particular, the components at frequencies near to fifth and seventh harmonics, produced by the interaction between the rotor faults and the harmonics of the spatial distribution of stator windings, are analyzed in this work. A multiple coupled circuit model of the induction motor is used to evaluate the sensitivity of these components for different stator winding configurations, load level, supply voltage conditions, and different number of broken bars. Simulation results showed that a particular analyzed component near to fifth harmonic depends mainly on fifth harmonic of winding distribution, which remains almost constant for most common distributions. Therefore, it is expected that this component should be found in most motors with broken bars. Finally, experimental laboratory results and two industrial cases that validate the analysis are presented.

1. Introduction

Fault diagnosis in electrical machines, particularly induction motors (IM), has been a very active research area in recent times [1]. This is mainly due to the importance of IM in industrial production processes. The use of fault detection strategies in conjunction with a predictive maintenance program contributes to reduce unscheduled downtime [2,3].

Particularly the detection and correct diagnosis of broken bars in IM is a problem that has received special attention, despite it does not represent the fault of higher occurrence [2,3]. An important variety of strategies have been proposed as options to the already accepted mechanical vibration analysis. Fault detection techniques based on current and voltage measurement, powers and fluxes have proved efficiency in fault detection and diagnosis processes, not only for faults originated electromagnetically but also mechanically [3–9]. Among these strategies, the motor current signature analysis (MCSA) is the most widespread, due its simplicity and minimum number of required sensors [9–13]. Most of these strategies use the magnitude of the sidebands at the fundamental component $(1 \pm 2s)f_s$ as fault indicator, where s is the slip and f_s the supply frequency [10,13]. Suitable fault severity factors have been proposed based on these sidebands [13]. However, the amplitude of these components not only depends on the fault severity, but it also depends on factors such as the load level and inertia of the motor-load set, among others [13–15]. Moreover, low-frequency oscillations in the load torque affect motor currents in a very similar way; that is, by introducing sidebands around the fundamental component. Situations of this nature hinder the correct quantification of the failure and may even induce false diagnosis [16].

Several proposals that pose solutions to these problems have been recently presented [17–21]. Some works propose strategies that require measurement of both, current and voltage [18], special sensors [19] or signals analysis during transient periods [21,22]. However, additional information to that provided by the components at frequencies $(1 \pm 2s)f_s$ can be extracted from the spectral analysis of a phase current, without resort to complex signals processing techniques nor additional sensors.

Particularly, the analysis of current components around high order harmonics has been proposed with the objective of improving rotor fault diagnosis [10,16]. In general, high frequency components are less sensitive to load oscillations due to the "filter" effect that inertia produces on oscillations. These high frequency components can be caused by the interaction between asymmetry on the rotor – due to broken bars – and either the harmonics due to supply voltage distortion or unbalances, or the spatial harmonics due to the stator windings distribution or the rotor slots harmonics (RSH) [23–27].

The use of the components due to supply voltage distortion or unbalance to generate rotor fault indicators was proposed and

* Corresponding author at: Grupo de Electrónica Aplicada, Facultad de Ingeniería, Universidad Nacional de Río Cuarto, Ruta Nac. No. 36 km 601, X5804BYA Río Cuarto, Córdoba, Argentina. Tel./fax: +54 358 4676598/4676255.
E-mail address: cpezzani@ing.unrc.edu.ar (C. Pezzani).

0957-4158/$ - see front matter © 2013 Elsevier Ltd. All rights reserved.
http://dx.doi.org/10.1016/j.mechatronics.2013.09.008

analyzed in [23]. Although these indicators are less sensitive to amplitude variations of voltage harmonics, it becomes necessary a certain degree of distortion. This can be quite easily achieved in inverter-fed motors. However, in motors supplied directly from the grid, it may not occur, even less in medium-voltage motors.

On the other hand, the use of components produced by a discrete distribution of the rotor (RSH) requires knowledge on some construction parameters such as the number of rotor bars and also an accurate estimate of the motor slip [24,25].

The non-sinusoidal distribution of windings produces spatial harmonics on magnetomotive force (*mmf*), mainly at frequencies given by $(6k \pm 1)f_s$, with $k = 1, 2, \ldots$ The interaction between these spatial harmonics and rotor asymmetry produces characteristic components in the current spectrum of the IM [26]. The components at frequencies $(5-4s)f_s$, $(5-6s)f_s$, $(7-6s)f_s$ and $(7-8s)f_s$, located around 5th and 7th harmonics, are the most significant ones [27]. The use of these components as potential indicators of broken bars has been presented in [26,27]. However, for any fault indicator, a deep analysis of the influence of the motor operation conditions as well as other factors must be done in order to determine their effectiveness and applicability for fault detection and identification. A first analysis of the behavior of the components $(5-4s)f_s$ and $(7-6s)f_s$, for different number of broken bars, load inertia variations and supply voltage conditions was presented in [28]. From this analysis it was demonstrated, for a particular winding distribution, the usefulness of the components $(5-4s)f_s$ and $(7-6s)f_s$ to support the broken bars diagnosis.

In this paper a detailed analysis of the components $(5-4s)f_s$ and $(7-6s)f_s$ as indicators of broken bars in the IM is presented. A multiple coupled circuit model of the IM [29,30] is used to evaluate the sensitivity of these components for different winding configurations. Through numerical simulation, the amplitude of fault indicators is evaluated in terms of the winding distribution harmonics using the proposed model. The influence of voltage distortion, inertia and load level is also analyzed. Finally, several experimental laboratory results and two industrial cases that validate the analysis are presented.

2. Induction motor model

The components of interest for broken bar detection are produced by the interaction between the spatial harmonics of the stator winding distribution and rotor asymmetry due to broken bars. Therefore it becomes necessary use a model that allows considering different stator windings and rotor distributions. In this work, multiple-coupled circuit model proposed in [29] is used with this aim and the winding function method is employed for inductances calculation [30]. This approach allows considering the actual distribution of stator windings and rotor bars and facilitates the inductances calculation for different motors types or under fault conditions [31–33]. Saturation effects and eddy currents are neglected in this formulation and the rotor bars are supposed to be isolated. In addition, stator teeth and rotor slots are neglected since their effect hardly affects the components of interest [34]. The inclusion of saturation effects on induction and synchronous machines models using the WFA has been recently proposed in [38–40]. However, as will be later demonstrated in Section 5.1.2, this effect on the components of interest is negligible.

In general, the IM consists of m stator circuits and k rotor bars. The squirrel-cage rotor can be modeled as k identical equally spaced loops constituted by two consecutive bars plus a current loop on one of the end-rings (Fig. 1) [29]. In Fig. 1, r_e and L_e are the resistance and leakage inductance of the end-ring segment, respectively. r_b is the rotor bar resistance and L_b is the rotor bar leakage inductance.

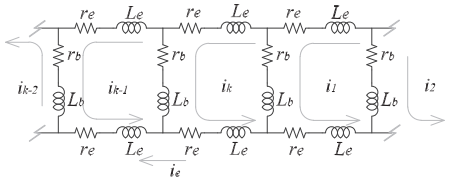

Fig. 1. Squirrel-cage equivalent circuit.

To calculate self and mutual inductances of the model, Modified Winding Function Approach [30] is used, which allows considering non-uniformity, both radial and axial, on windings and on the air–gap. This makes it possible to analyze the effects of winding distribution, skew and the variations in the air–gap due to either eccentricity or rotor and stator slots simultaneously. Mutual inductance between any two circuits, A and B of the motor can be calculated as,

$$L_{BA}(\theta_r) = \mu_0 r \int_0^{2\pi} \int_0^{L} n_B(\phi, z, \theta_r) N_A(\phi, z, \theta_r) g^{-1}(\phi, z, \theta_r) dz d\phi, \quad (1)$$

where μ_0 is vacuum permeability, r is the mean radius of the air gap, ϕ and z are angular and axial positions corresponding to an arbitrary point in the air gap and $g^{-1}(\phi, z, \theta_r)$ is the inverse of the air–gap function. For circuit "j" $n_j(\phi, z, \theta_r)$ and $N_j(\phi, z, \theta_r)$ are the "Winding Spatial Distribution" and the "Winding Modified Two-dimensional Function", respectively.

The latter can be expressed as,

$$N_j(\phi, z, \theta_r) = n_j(\phi, z, \theta_r) - 1/2\pi L \langle g^{-1}(\phi, z, \theta_r) \rangle \int_0^{2\pi} \int_0^{L} n_j(\phi, z, \theta_r) g^{-1}(\phi, z, \theta_r) dz d\phi \quad (2)$$

where $\langle g^{-1}(\phi, z, \theta_r) \rangle$ is the mean value of the air–gap function inverse.

2.1. Calculation of inductances

From (1) and (2), it is possible to determine the coupling inductance between each circuit of the IM. One way to accomplish this is through expressing the winding functions by Fourier series. This also allows analyzing each spatial distribution harmonic separately. Below, the distribution of windings using Fourier series is widely discussed and the calculation of rotor and stator mutual inductances presented.

2.1.1. Windings distribution of stator and rotor circuits

Fig. 2 shows the distribution of the stator windings corresponding to phase a for a winding with full pitch and equal number of turns in all coils. In this figure, γ is the pitch and q is the number of coils per pole, N_t is the number of turns per phase and per pole and P is the number of pole pairs. The stator slots pitch γ is represented by,

$$\gamma = 2\pi / R_s, \quad (3)$$

where R_s is the number of stator slots.

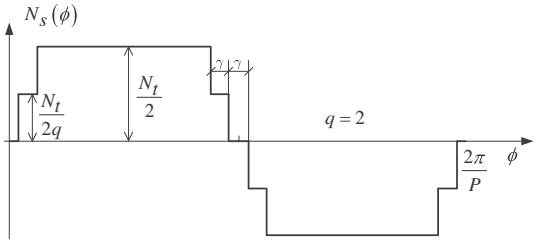

Fig. 2. Winding distribution. Particular case with $q = 2$.

Through analyzing the distribution of windings in a similar way to [35], it is possible to express winding function for the stator circuits in Fourier series as shown in (4).

$$N_s(\phi) = \frac{2}{\pi} N_t \sum_{n=1}^{\infty} \frac{k_{dn} k_{pn}}{n} \sin(nP\phi) \quad n \text{ odd}, \tag{4}$$

where k_{dn} and k_{pn} are the distribution factor and pitch factor, respectively. They are given by:

$$k_{dn} = \sin(nqP\gamma/2)/q \sin(nP\gamma/2) \quad n \text{ odd}, \tag{5}$$

$$k_{pn} = \cos(nqP\gamma/2) \quad n \text{ odd}. \tag{6}$$

From (4), it can be observed that the amplitude of each harmonic corresponding to the windings distribution is given by the expression:

$$k_n = 2N_t k_{dn} k_{pn}/\pi n \qquad n \text{ odd}. \tag{7}$$

As it can be seen, the amplitude of each harmonic directly depends on the winding distribution (factors k_{dn}, k_{pn}).

Equation (4) represents the winding function for a stator phase under uniform air–gap conditions. In the case of three-phase IM, the functions of the remaining phases are obtained by shifting the previous function by $\pm\frac{2}{3}\pi$.

Fig. 3 shows, in dashed line, the winding distribution ($n_r(\theta_r, \phi)$) for a rotor loop. In this figure ϕ is a particular angular position along the stator and θ_r is the rotor angle with respect to a fixed stator point. Considering axial uniformity (without skewing) the winding distribution can be expressed as:

$$n_r(\theta_r, \phi) = \begin{cases} 0 & 0 < \phi \leqslant \theta_r - \alpha_r/2 \\ 1 & \theta_r - \alpha_r/2 < \phi \leqslant \theta_r + \alpha_r/2 \\ 0 & \theta_r + \alpha_r/2 < \phi \leqslant 2\pi \end{cases}, \tag{8}$$

where

$$\alpha_r = 2\pi/k, \tag{9}$$

is the rotor slots pitch and k is the number of rotor slots and bars.

Considering air–gap uniformity, the winding function for the rotor loop results:

$$N_r(\theta_r, \phi) = \begin{cases} -\alpha_r/2\pi & 0 < \phi \leqslant \theta_r - \alpha_r/2 \\ 1 - \alpha_r/2\pi & \theta_r - \alpha_r/2 < \phi \leqslant \theta_r + \alpha_r/2 \\ -\alpha_r/2\pi & \theta_r + \alpha_r/2 < \phi \leqslant 2\pi. \end{cases} \tag{10}$$

The winding function (10) is shown in solid line in Fig. 3.

2.1.2. Example of calculation of inductance L_{sr}

From the winding functions (4) and (8) of the stator circuits and rotor loops, it is possible to determine the self and mutual inductances of the motor. As an example, the expression of the coupling inductance between the stator winding and a rotor loop is presented in (11). By replacing (4) and (10) into (1), it is obtained,

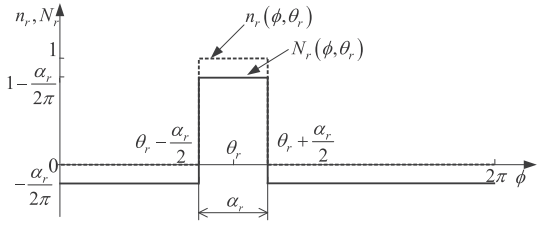

Fig. 3. Spatial winding distribution and winding function, corresponding to a rotor loop.

$$L_{sr}(\theta_r) = \frac{2\mu_0 rL}{gP^2} \sum_{n=1}^{\infty} \frac{k_n k_{bn}}{n} \sin(nP\theta_r) \quad n \text{ odd}, \tag{11}$$

where

$$k_{bn} = \sin(nP\alpha_r/2). \tag{12}$$

3. Frequency components related to broken bars

The interaction between the asymmetry produced by broken bars and the spatial harmonics of the windings distribution introduces high frequency components in the machine currents spectrum. These components appear at frequencies given by [26]:

$$f_{stator,bb} = \left[\left(\frac{\eta}{P} \mp n\right)(1-s) \pm 1\right] f_s \tag{13}$$

where n is the order of the spatial harmonic of the stator–rotor mutual inductance, and $\eta = 1, 2, \ldots$

From the components predicted by (13), those at $(5-4s)f_s$, $(5-6s)f_s$, $(7-6s)f_s$ and $(7-8s)f_s$ frequencies are the most significant. The components at $(5-4s)f_s$, and $(7-6s)f_s$ are mainly due to the 5th harmonic of the stator winding distribution ($n = 5$), whereas the rest of them are due to the 7th harmonics ($n = 7$) [27].

As shown in the previous section (Eq. (7)), the amplitude of each winding distribution harmonic is directly dependent on the characteristics of such distribution. In the same way, for a given rotor configuration ($k_{bn} = ctte$), the amplitude of space harmonics of the stator-rotor mutual inductance (Eq. (11)) directly depends on k_n, and therefore on the winding distribution.

Table 1 shows the fifth-harmonic component of the winding distribution in percent of the fundamental component for several distributions. Among three-phase motors, the most commonly used "*phase belt*" is 60° and, in some cases, 120° [36,37]. On the other hand, for two-phase motors, 90° is generally used and 180° in some cases. As it can be seen from the results shown in this table, for most common distributions, the fifth-harmonic amplitude with respect to the fundamental component does not change significantly with an increase in the number of coils per pole, q.

From Table 1 and Eq. (11) it can be concluded that, if the fifth harmonic of the winding distribution does not vary significantly from one distribution to another, then the fifth harmonic of the mutual inductance will not vary. Therefore, it is expected that the components at $(5-4s)f_s$ and $(7-6s)f_s$ can be found in most motors with a rotor fault, since they directly depend on the 5th harmonic of the stator winding distribution. This suggests that components $(5-4s)f_s$ and $(7-6s)f_s$ can be used as a complement to traditional indicators (sidebands at $(1 \pm 2s)f_s$) for a correct diagnosis of rotor faults.

4. Simulation analysis

Through using the model proposed in Section 2, the IM was simulated with rotor asymmetry. To analyze the behavior of the $(5-4s)f_s$ and $(7-6s)f_s$ stator current components, simulation

Table 1
Fifth-harmonic component of the winding distribution (%).

q	Phase belt ($2Pq\gamma$)			
	60°	90°	120°	180°
1	5.359	8.284	20.000	20.000
2	4.288	4.692	5.359	8.284
3	4.124	4.288	4.533	5.359
4	4.069	4.158	4.288	4.692
5	4.044	4.100	4.181	4.424
∞	4.000	4.000	4.000	4.000

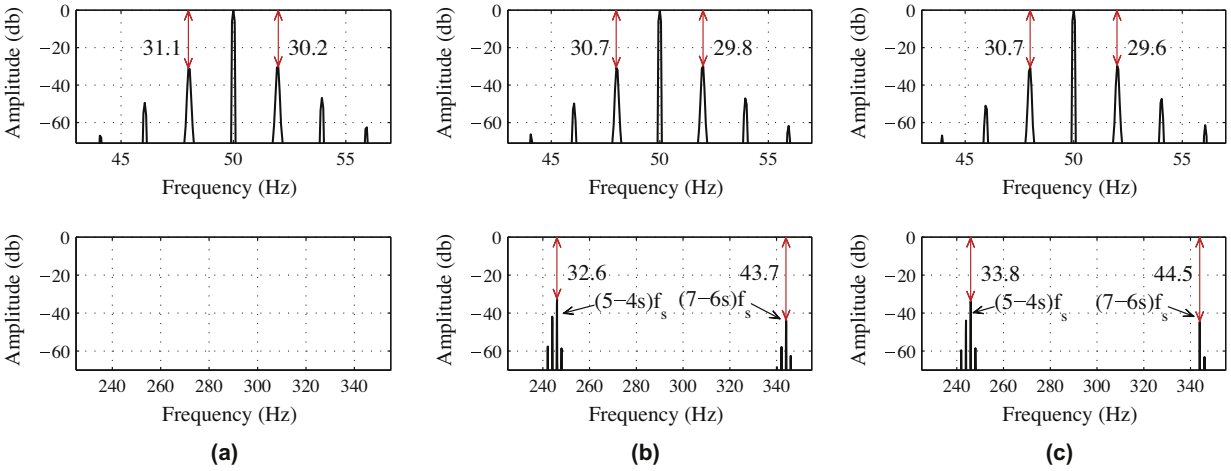

Fig. 4. Sidebands $(1 \pm 2s)f_s$ and components $(5 - 4s)f_s$ and $(7 - 6s)f_s$ for three broken bars: (a) sinusoidal winding distribution, (b) fifth-harmonic in the winding distribution, (c) real winding distribution (Simulation).

results for different conditions regarding winding distribution, load, number of broken bars, inertia of the machine-load unit and voltage distortion are obtained and presented in this section. For the sake of comparison, the behavior of sidebands around the fundamental component of the current is shown too.

The breakage of either one or more bars or a section of the end-ring was included in the model as presented in [33], i.e. by eliminating the equation of the rotor loop corresponding to the broken bar. To model an incipient fault (a partially broken bar), the resistance of the faulty bar was increased. Due to an increase of the bar resistance of 10 times produces a similar effect of a completely broken bar; an increase of 3.5 times was used for the simulation of an incipient fault. The data and parameters of the motor used are listed in Table A.1 in Appendix A.

4.1. Winding distribution

Fig. 4 shows the frequency spectra corresponding to a current for three broken bars and different winding distributions. For the three cases shown, a balanced sinusoidal supply voltage and a 100% load are applied.

Fig. 4(a) shows the frequency spectrum around the fundamental component as well as around the fifth and seventh harmonics, for the sinusoidal distribution case. In this figure sidebands at $(1 \pm 2s)f_s$, typical for rotor faults [10,13], are observed. Because the 5th harmonic of the winding distribution was not included in the model, components at $(5 - 4s)f_s$ and $(7 - 6s)f_s$ do not appear in the spectrum. Fig. 4(b) shows the results obtained from incorporating the fifth-harmonic component to the winding distri-

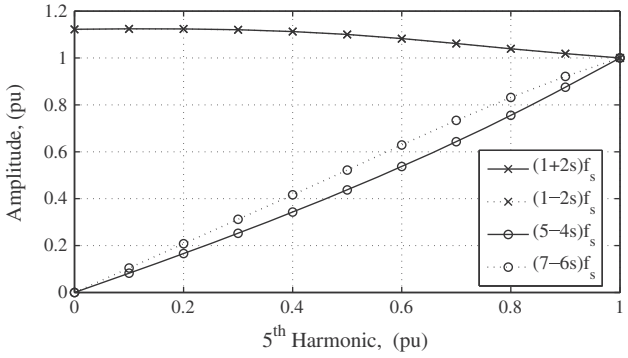

Fig. 5. Amplitude of sidebands $(1 \pm 2s)f_s$ and components $(5 - 4s)f_s$ and $(7 - 6s)f_s$, as a function of the 5th harmonic of the winding distribution for three broken bars (Simulation).

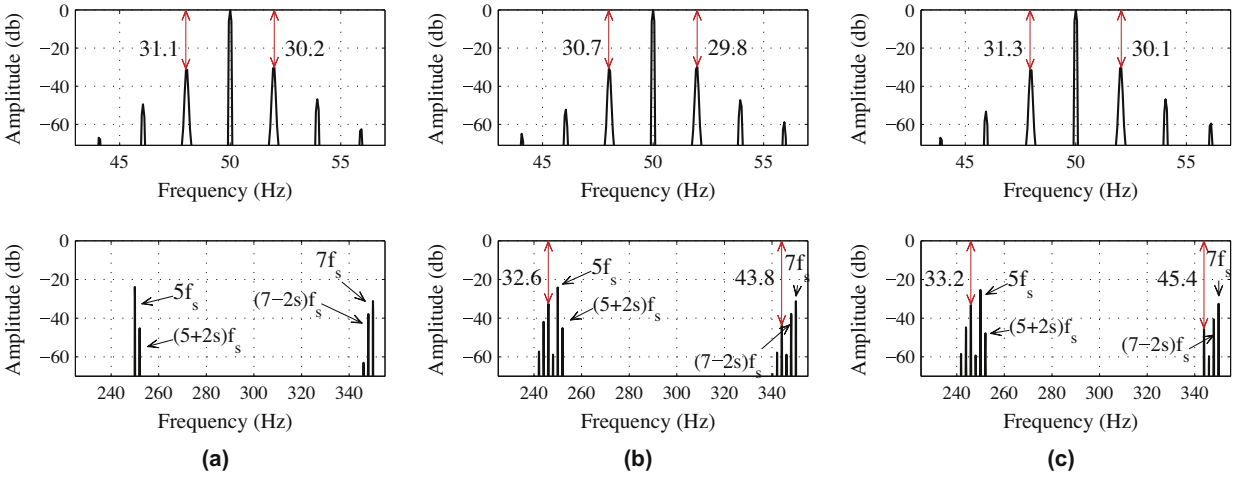

Fig. 6. Sidebands $(1 \pm 2s)f_s$ and components $(5–4s)f_s$ and $(7–6s)f_s$ for three broken bars and voltage distortion: (a) sinusoidal winding distribution, (b) 5th harmonic in winding distribution, (c) real winding distribution (Simulation).

bution. This component hardly affects the amplitude of the sidebands around the fundamental component, but it produces new components in the frequency spectrum at $(5-4s)f_s$ and $(7-6s)f_s$. Finally, Fig. 4(c) shows the simulation results considering all the harmonics of the winding distribution. As it can be observed, the incorporation of all distribution harmonics does not significantly change the amplitude of the analyzed components.

Fig. 5 shows the amplitude of the sidebands around the fundamental frequency and the 5th and 7th harmonics, as a function of the amplitude of the 5th harmonic of the winding distribution for three broken bars. The values of the horizontal axis are expressed in per-unit of the 5th harmonic of the actual machine winding distribution (see Table A.1). These results correspond to the motor with sinusoidal voltage and rated load. It can be observed that the components at $(1\pm2s)f_s$ frequency do not significantly vary with the fifth-harmonic component of the winding distribution whereas the components at $(5-4s)f_s$ and $(7-6s)f_s$ frequencies do almost linearly.

4.2. Harmonic voltage distortion

To analyze the effects of voltage harmonic distortion on the analyzed components, the IM was simulated under the same conditions as the previous case (Fig. 4) but including voltage distortion. Fig. 6 show the results obtained with 5% of the 5th harmonic voltage and a 3% 7th harmonic voltage. In Fig. 6 (a), it can be seen that the components around the fundamental one do not changed due to voltage distortion. Around the harmonics, as it was analyzed in [23], new useful components at $(5+2s)f_s$ and $(7-2s)f_s$ frequencies appear even for a sinusoidal distribution of windings. Fig. 6(b) shows the results incorporating the 5th harmonic in the winding distribution; the components at $(5-4s)f_s$ and $(7-6s)f_s$ frequencies mentioned above can also be observed. From comparing Fig. 6(a) and (b), it can be deduced that the 5th harmonic component of winding distribution does not produce significant changes on the components at $(5+2s)f_s$ and $(7-2s)f_s$ frequencies. Similarly, from comparing Figs. 4(b) and 6(b), it can be seen that voltage distortion hardly affects the components at $(5-4s)f_s$ and $(7-6s)f_s$ frequencies. Fig. 6(c) shows the results obtained considering all the harmonics of the winding distribution. As in the previous case, it can be observed that including all the harmonics do not significantly affect the components under study in the stator current spectrum.

4.3. Number of broken bars

In general, for any component used for fault detection and identification it is desirable that it helps quantifying the fault severity. Fig. 7 shows the amplitude of the sidebands around the fundamental component as well as the components $(5-4s)f_s$ and $(7-6s)f_s$ for a motor with an incipient fault (a partially broken rotor bar), one, two and three broken bars. In all these cases, the motor works with rated load. It can be observed in the same figure that all the components increase as the number of broken bars does. The component at frequency $(7-6s)f_s$ does not show such increase between two and three broken bars, thus, it is a good indicator to support the rotor fault detection but not to evaluate the fault severity. Furthermore, the component at frequency $(5-4s)f_s$ is a good indicator of the fault severity.

4.4. Motor-load inertia

Fig. 8 shows the behavior of the sidebands around the fundamental current and near to current harmonics as a function of inertia of the motor-load unit. From previous statements, the upper sideband, $(1+2s)f_s$, is produced by motor speed oscillations. Then,

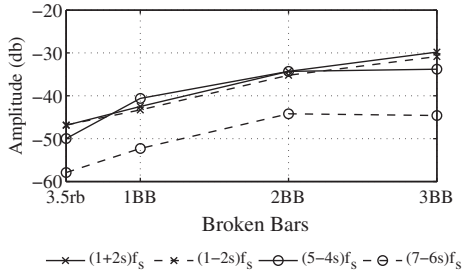

Fig. 7. Amplitude of sidebands $(1\pm2s)f_s$ and components $(5-4s)f_s$ and $(7-6s)f_s$ as a function of the rotor fault severity (Simulation).

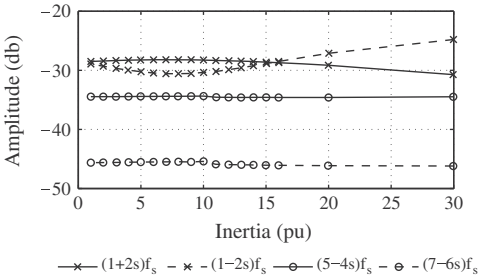

Fig. 8. Amplitude of sidebands $(1\pm2s)f_s$ and components $(5-4s)f_s$ and $(7-6s)f_s$ as a function of inertia for 3 broken bars. Rated load (Simulation).

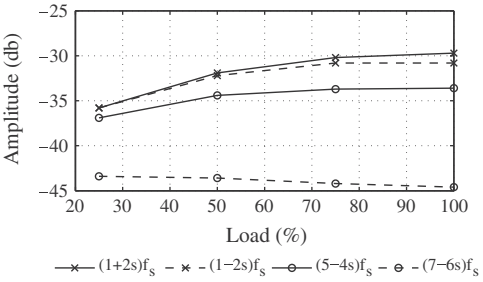

Fig. 9. Amplitude of sidebands $(1\pm2s)f_s$ and components $(5-4s)f_s$ and $(7-6s)f_s$ as a function of load for 3 broken bars (Simulation).

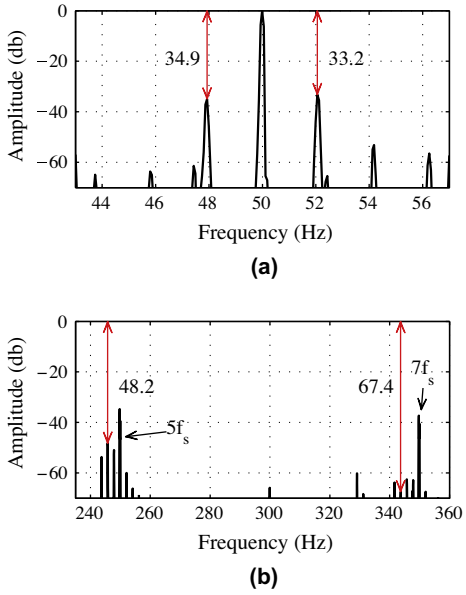

Fig. 10. Frequency spectrum around (a) the fundamental component and (b) around 5th and 7th harmonics for three broken bars. (Laboratory results).

as inertia increases significantly, this component tends to zero while the lower sideband increases. However, for this case, the amplitude of the lower sideband is higher than that of the upper sideband only for inertia values fifteen times higher than those of the motor. Results obtained for inertia values up to twelve times the motor inertia, are similar to those obtained by [13]. On the contrary, the components at $(5-4s)f_s$ and $(7-6s)f_s$ frequencies do not practically vary with inertia, as it can be observed in Fig. 8.

4.5. Influence of motor load

Fig. 9 shows the behavior of the sidebands at $(1\pm 2s)f_s$ and near to current harmonics as a function of the motor load for 3 broken bars. In the particular case of the motor running at no load, the rotor currents are almost zero and then the breakage of bars cannot be detected from stator currents. As load increases, the amplitude of all components also increases while they separate from the fundamental component and the harmonics. This makes it easier to recognize them all.

5. Experimental validation

In order to validate the simulation results shown in the previous section, laboratory tests under different operation conditions were performed. In addition, two industrial cases with broken bars were analyzed. For the laboratory experiments four different rotors were used: a healthy rotor and three rotors with one, two and three broken bars (see Fig. B.1 in Appendix B). Two phase currents were measured and registered with an oscillographic recorder. The technical data of the motor used as well as the data related to the winding distribution are shown in Table A.1 in Appendix A.

5.1. Laboratory results

Fig. 10 shows the frequency spectrum around the fundamental current and near the 5th and 7th harmonics for a motor with three broken bars and rated load. Fig. 10(b) shows the components at $(5-4s)f_s$ and $(7-6s)f_s$ frequencies produced by rotor faults. From the same figures it can be observed that these components appear

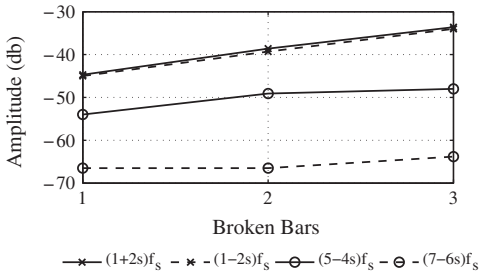

Fig. 11. Amplitude of sidebands $(1\pm 2s)f_s$ and components $(5-4s)f_s$ and $(7-6s)f_s$ as a function of the number of broken bars; motor working at rated load (Laboratory results).

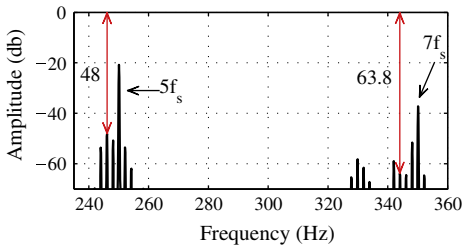

Fig. 12. Components $(5-4s)f_s$ and $(7-6s)f_s$ for three broken bars and harmonic distortion (5% of the 5th harmonic and 1.1% of the 7th) (Laboratory results).

even when the motor is fed with voltages with low distortion (THD < 1%).

Fig. 11 shows the amplitudes of the sidebands as a function of the number of broken bars. As it can be seen, these amplitudes grow with the number of broken bars. Comparing Figs. 11 and 7, it can be observed that the amplitudes at $(5-4s)fs$ and $(7-6s)f_s$ obtained experimentally are lower than those obtained by simulation, especially the amplitude of the component at $(7-6s)f_s$.

5.1.1. Voltage harmonic distortion

To evaluate the sensitivity of the components $(5-4s)f_s$ and $(7-6s)f_s$ against voltage distortion, the analysis of the currents

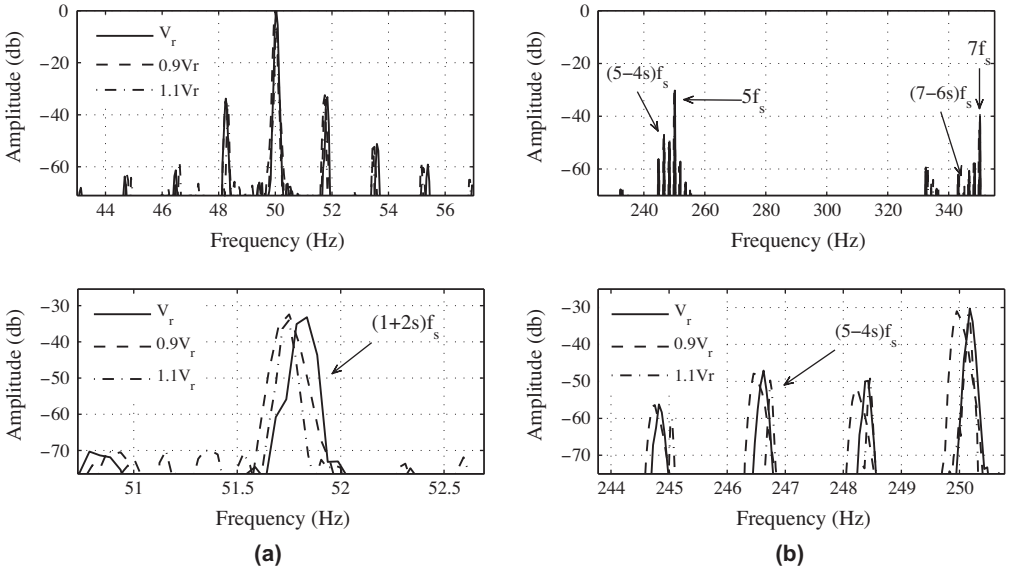

Fig. 13. Amplitude of sidebands $(1\pm 2s)f_s$ (a) and components $(5-4s)f_s$ and $(7-6s)f_s$ (b), for a motor with 2 broken bars supplied with undervoltage (0.9 Vr) and overvoltage (1.1 Vr) (Laboratory results).

for the motor with three broken bars and distorted voltage (5% 5th and 1.1% 7th) was carried out. Fig. 12 shows the spectrum around the 5th and 7th current harmonic. From this figure, it can be observed that there are no significant changes in the components at $(5-4s)f_s$ and $(7-6s)f_s$ frequencies with respect to the result with lower harmonic distortion, previously shown in Fig. 10(b).

5.1.2. Undervoltage and overvoltage

A high level of saturation in the iron can reduce the effect of the broken bars on the stator currents [41]. According to [41], this effect produces a reduction in the amplitude of the characteristic components of the fault and must be taken into consideration for precise quantification of the fault severity. For such reason, experimental results with different levels of saturation in the iron were obtained. The effects of saturation over the $(5-4s)f_s$ and $(7-6s)f_s$ current components were evaluated by supplying the motor with two broken bars with 10% of overvoltage in a first test, and 10% undervoltage in a second one. Fig. 13 shows the spectrum around the fundamental component (Fig. 13(a)) and 5th and 7th current harmonics (Fig. 13(b)) for rated voltage (V_r), over and under voltage. At the bottom of each figure, a detail of the fault characteristic components is shown. As it can be appreciated in Fig. 13, even when the voltage is ±10% V_r, the amplitudes of the $(5-4s)f_s$ and $(7-6s)f_s$ components are almost the same as for the rated voltage case. For the tested IM, this result shows that there are not significant variations in the amplitude of the diagnostic components with the saturation level.

5.1.3. Low-frequency load oscillations

As a final test, a healthy motor was coupled to an IM drive which acts as a programmable load. The torque of this drive was controlled, with torque reference composed by a constant value plus an oscillating torque. Fig. 14 shows the obtained results for a motor with a pulsating load (75% load and oscillating load of 3.5% at 2 Hz). Sidebands at $(1\pm 2s)f_s$ (Fig. 14(a)) are very similar to those produced by broken bars (Fig. 10(a)). However, as opposed to the broken bar case, components at $(5-4s)f_s$ and $(7-6s)f_s$ does not appear in the spectrum of the oscillating load case, as can be seen in Fig. 14(b). These results validate the fact that the sidebands around the harmonic components are useful to identify and separate rotor faults from oscillations produced by the load, mainly in those cases where the oscillating load frequency is close to $2sf_s$.

5.2. Industrial cases

The usefulness of components $(5-4s)f_s$ and $(7-6s)f_s$ as indicators of broken bars was also tested on different motors working in industrial plants. Two motors with broken bars and different characteristics were analyzed. *Motor 1* corresponds to a 55 kW IM with several broken bars, that drives an auxiliary pump in a combined

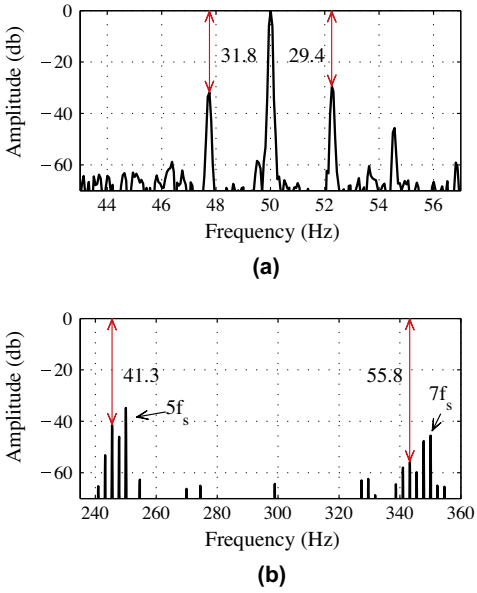

Fig. 15. Frequency spectrum around (a) the fundamental component and (b) around 5th and 7th harmonics for a motor with several broken bars (*Industrial case. Motor 1*).

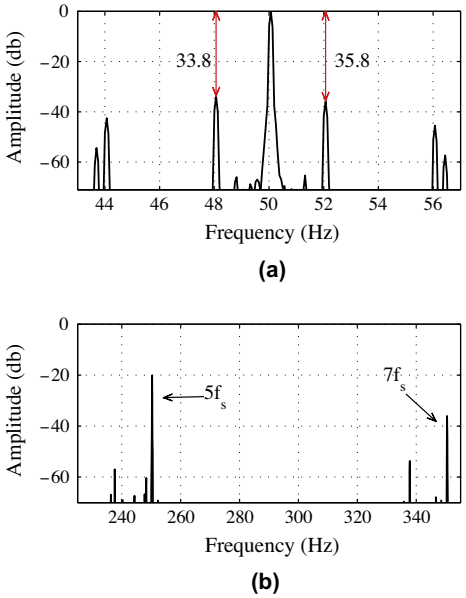

Fig. 14. Frequency spectrum for a healthy motor with 75% load, and oscillating load of 3.5% at 2 Hz, (a) around the fundamental component, (b) around 5th and 7th harmonics (Laboratory results).

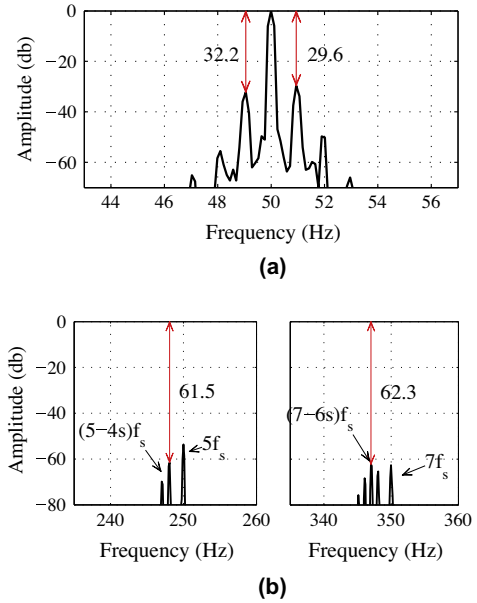

Fig. 16. Frequency spectrum around (a) the fundamental component and (b) around 5th and 7th harmonics for a motor with broken bars (*Industrial case. Motor 2*).

cycle power plant. The nameplate data of the IM are presented in Table A.2 in the Appendix A. Fig. 15 shows the frequency spectrum around the fundamental current and near 5th and 7th harmonics, with the motor at rated load. The components at $(5-4s)f_s$ and $(7-6s)f_s$ frequencies produced by rotor faults can be observed in Fig. 15(b).

Motor 2 corresponds to a 1656 kW IM that drives a high-pressure pump. The results obtained from this motor, operating at 90% load, are shown in Fig. 16. The nameplate data of this machine are presented in Table A.2 in Appendix A. In this case, current was measured in the secondary of the corresponding current measurement transformer. The current spectrum (Fig. 16(a)) shows sidebands that can be produced by broken rotor bars. Fig. 16(b) shows the components at $(5-4s)f_s$ and $(7-6s)f_s$ frequencies produced by rotor faults.

6. Conclusions

Rotor faults produce frequency components other than sidebands around the fundamental component. The most significant components are generally located near the 5th and 7th harmonics. The components at frequencies $(5-4s)f_s$ and $(7-6s)f_s$ are mainly due to non-sinusoidal winding distribution and can be very useful in rotor fault diagnosis. In this paper, the behavior of these components as indicators of broken rotor bars in induction motors was deeply analyzed. It was demonstrated that for most commonly used configurations of windings, the 5th harmonic component of the spatial distribution of windings practically remains unchanged. From these results we can conclude that components $(5-4s)f_s$ and $(7-6s)f_s$, which depend mainly on the 5th harmonic and on the asymmetry caused by fault, should be present in most motor with rotor fault. Simulation and experimental results showed that components $(5-4s)f_s$ and $(7-6s)f_s$ increase with the number of broken bars while they are practically independent on the inertia of the motor-load unit. It was also demonstrated that these components are hardly affected by distortion or unbalance in the supply voltages. From both components, the one at $(5-4s)f_s$ is the most significant and useful for detection and diagnosis. In case of motors fed by distorted voltages, the analysis of these components can be combined with the components produced by the interaction between voltage distortion and rotor asymmetry to support the rotor fault diagnosis. A great advantage of the proposed strategy is that it can be used for condition monitoring in an industrial plant, with a minimum knowledge of the motor data and only one current sensor.

Appendix A

Technical data and parameters of the IM are shown in Table A.1 and A.2.

Table A.1
IM technical data and parameters for simulation and laboratory results.

Induction Motor	
Rated Power	5.5 kW
Rated Voltage	380 V
Rated Frequency (f_s)	50 Hz
Rated Current	11.1 A
Rated speed	1470 rpm
Power Factor	0.85
Stator Winding	18 turns per coil, 2 coil per group, 4 group per phase, series connection, step 1:10:12;
Stator Slots	48
Rotor Bars	40
Skewing	0.8 p.r.r.
Inertia	0.02 kg m^2

Table A.2
IM technical data for industrial cases results.

	Motor 1	Motor 2
Power (kW)	55	1656
Voltage (V)	380	2300
Frequency (f_s) (Hz)	50	50
Rated current (A)	100	475
Rated speed (rpm)	1475	1488
Power factor	0.88	0,91
Rotor bars	40	76

Appendix B

Induction motor rotors for laboratory results are shown in Fig. B.1.

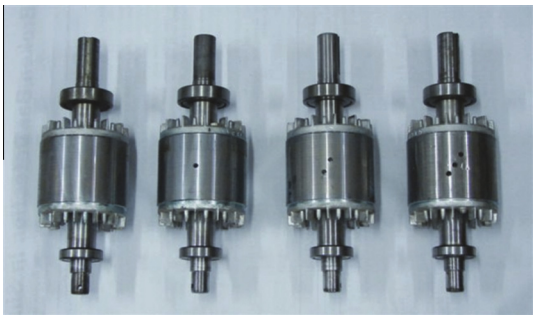

Fig. B.1. Induction motor rotors: healthy, one, two and three broken bars.

References

[1] Capolino GA, Filippetti F. Introduction to the special section on advances in diagnosis for electrical machines, power electronics, and drives – Part I. IEEE Trans Ind Electron 2013;60:3396–7.
[2] Nandi S, Toliyat HA, Xiaodong L. Condition monitoring and fault diagnosis of electrical motors – a review. IEEE Trans Energy Convers 2005;20:719–29.
[3] Bellini A, Filippetti F, Tassoni C, Capolino GA. Advances in diagnostic techniques for induction machines. IEEE Trans Ind Electron 2008;55:4109–26.
[4] Faiz J, Ojaghi M. Different indexes for eccentricity faults diagnosis in three-phase squirrel-cage induction motors: a review. Mechatronics 2009;19:2–13.
[5] Pires DF, Pires VF, Martins JF, Pires AJ. Rotor cage fault diagnosis in three-phase induction motors based on a current and virtual flux approach. Energy Convers Manage 2009;50:1026–32.
[6] Çalış H, Çakır A. Experimental study for sensorless broken bar detection in induction motors. Energy Convers Manage 2008;49:854–62.
[7] Ceban A, Pusca R, Romary R. Study of rotor faults in induction motors using external magnetic field analysis. IEEE Trans Ind Electron 2012;59:2082–93.
[8] Soualhi A, Clerc G, Razik H. Detection and diagnosis of faults in induction motor using an improved artificial ant clustering technique. IEEE Trans Ind Electron 2013;60:4053–62.
[9] El Hachemi Benbouzid M. A review of induction motors signature analysis as a medium for faults detection. IEEE Trans Ind Electron 2000;47:984–93.
[10] Kliman GB, Koegl RA, Stein J, Endicott RD, Madden MW. Noninvasive detection of broken rotor bars in operating induction motors. IEEE Trans Energy Convers 1988;3:873–9.
[11] Joksimovic GM, Riger J, Wolbank TM, Peric N, Vasak M. Stator-current spectrum signature of healthy cage rotor induction machines. IEEE Trans Ind Electron 2013;60:4025–33.
[12] Yong-Hwa K, Young-Woo Y, Don-Ha H, Jong-Ho S, Dong-Sik K. High-resolution parameter estimation method to identify broken rotor bar faults in induction motors. IEEE Trans Ind Electron 2013;60:4103–17.
[13] Bellini A, Filippetti F, Franceschini G, Tassoni C, Kliman GB. Quantitative evaluation of induction motor broken bars by means of electrical signature analysis. IEEE Trans Ind Applic 2001;37:1248–55.
[14] Concari C, Franceschini G, Tassoni C, Toscani A. Validation of a faulted rotor induction machine model with an insightful geometrical interpretation of physical quantities. IEEE Trans Ind Electron 2013;60:4074–83.
[15] Faiz J, Ebrahimi BM, Toliyat HA, Abu-Elhaija WS. Mixed-fault diagnosis in induction motors considering varying load and broken bars location. Energy Convers Manage 2010;51:1432–41.
[16] Schoen RR, Habetler TG. Effects of time-varying loads on rotor fault detection in induction machines. IEEE Trans Ind Applic 1995;31:900–6.
[17] Aydin I, Karakose M, Akin E. A new method for early fault detection and diagnosis of broken rotor bars. Energy Convers Manage 2011;52:1790–9.

[18] Bossio G, De Angelo C, Bossio JM, Pezzani CM, García GO. Separating broken rotor bars and load oscillations on im fault diagnosis through the instantaneous active and reactive currents. IEEE Trans Ind, Electron 2009.
[19] Cabanas MF, Pedrayes F, Melero MG, Garcia CHR, Cano JM, Orcajo GA, et al. Unambiguous detection of broken bars in asynchronous motors by means of a flux measurement-based procedure. IEEE Trans Instrum Measure 2011;60:891–9.
[20] Bossio JM, De Angelo C, Bossio G. Self-organizing map approach for classification of mechanical and rotor faults on induction motors. Neural Comput Applic 2013;23:41–51.
[21] Pineda-Sanchez M, Riera-Guasp M, Roger-Folch J, Antonino-Daviu JA, Perez-Cruz J, Puche-Panadero R. Diagnosis of induction motor faults in time-varying conditions using the polynomial-phase transform of the current. IEEE Trans Ind Electron 2011;58:1428–39.
[22] Widodo A, Yang B-S, Gu D-S, Choi B-K. Intelligent fault diagnosis system of induction motor based on transient current signal. Mechatronics 2009;19:680–9.
[23] Bruzzese C. Analysis and application of particular current signatures (symptoms) for cage monitoring in nonsinusoidally fed motors with high rejection to drive load, inertia, and frequency variations. IEEE Trans Ind Electron 2008;55:4137–55.
[24] Bellini A, Yazidi A, Filippetti F, Rossi C, Capolino GA. High frequency resolution techniques for rotor fault detection of induction machines. IEEE Trans Ind Electron 2008;55:4200–9.
[25] Khezzar A, Kaikaa MY, El Kamel Oumaamar M, Boucherma M, Razik H. On the use of slot harmonics as a potential indicator of rotor bar breakage in the induction machine. IEEE Trans Ind Electron 2009;56:4592–605.
[26] Henao H, Razik H, Capolino GA. Analytical approach of the stator current frequency harmonics computation for detection of induction machine rotor faults. IEEE Trans Ind Applic 2005;41:801–7.
[27] Sobczyk TJ, Maciolek W. Diagnostics of rotor-cage faults supported by effects due to higher MMF harmonics. IEEE Power Technol Conf Proc, Bologna 2003;2:5.
[28] Bossio GR, De Angelo CH, Pezzani CM, Bossio JM, Garcia GO. Evaluation of harmonic current sidebands for broken bar diagnosis in induction motors. In: IEEE international symposium on diagnostics for electric machines, power electronics and drives (SDEMPED 2009); 2009. p. 1–6.
[29] Xiaogang L, Yuefeng L, Toliyat HA, El-Antably A, Lipo TA. Multiple coupled circuit modeling of induction machines. IEEE Trans Ind Applic 1995;31:311–8.
[30] Bossio G, De Angelo C, Solsona J, Garcia G, Valla MI. A 2-D model of the induction machine: an extension of the modified winding function approach. IEEE Trans Energy Convers 2004;19:144–50.
[31] Rajalakshmi Samaga BL, Vittal KP. Comprehensive study of mixed eccentricity fault diagnosis in induction motors using signature analysis. Int J Electr Power Energy Syst 2012;35:180–5.
[32] Obe ES, Binder A. Direct-phase-variable model of a synchronous reluctance motor including all slot and winding harmonics. Energy Convers Manage 2011;52:284–91.
[33] Toliyat HA, Lipo TA. Transient analysis of cage induction machines under stator, rotor bar and end ring faults. IEEE Trans Energy Convers 1995;10:241–7.
[34] Nandi S. Modeling of induction machines including stator and rotor slot effects. IEEE Trans Ind Applic 2004;40:1058–65.
[35] Lipo TA. Introduction to AC machine design. WI, USA: Madison; 1996.
[36] Alger PL. Induction machines: their behavior and uses. 2nd ed. Basel, Switzerland: Gordon and Breach; 1995.
[37] Cochran PL. Polyphase induction motors: analysis, design, and application. 1st ed. CRC Press; 1989.
[38] Hemmati S, Kojoori SS, Saied S, Lipo TA. Modelling and experimental validation of internal short-circuit fault in salient-pole synchronous machines using numerical gap function including stator and rotor core saturation. Electric Power Applic, IET 2013;7:391–9.
[39] Ghoggal A, Sahraoui M, Zouzou SE, Razik H. A fast inductance computation devoted to the modeling of healthy, eccentric, and saturated induction motors. Electric Power Compon Syst 2013;41:1002–22.
[40] Ghoggal A, Zouzou SE, Razik H, Sahraoui M, Hadri-Hamida A. Application of the convolution theorem for the modeling of saturated induction motors. In: 36th annual conference on IEEE industrial electronics society (IECON 2010); 2010. p. 772–7.
[41] Sprooten J, Maun JC. Influence of saturation level on the effect of broken bars in induction motors using fundamental electromagnetic laws and finite element simulations. IEEE Trans Energy Convers 2009;24:557–64.